Spectral-domain optical coherence phase and multiphoton microscopy

Chulmin Joo

Department of Mechanical Engineering, Massachusetts Institute of Technology, Cambridge, Massachusetts 02139, USA, and Wellman Center for Photomedicine, Massachusetts General Hospital, Boston, Massachusetts 02114, USA

Ki Hean Kim and Johannes F. de Boer

Wellman Center for Photomedicine, Massachusetts General Hospital, Boston, Massachusetts 02114, USA

We describe simultaneous quantitative phase contrast and multiphoton fluorescence imaging by combined spectral-domain optical coherence phase and multiphoton microscopy. The instrument employs two light sources for efficient optical coherence microscopic and multiphoton imaging and can generate structural and functional images of transparent specimens in the epidirection. Phase contrast imaging exhibits spatial and temporal phase stability in the subnanometer range. We also demonstrate the visualization of actin filaments in a fixed cell specimen, which is confirmed by simultaneous multiphoton fluorescence imaging. © 2007 Optical Society of America

OCIS codes: 110.0180, 110.4500, 180.3170, 180.2520.

Over the past decade, the development of quantitative phase imaging modalities has drawn increasing research interest because the nanoscale quantitative measurements on biological structures and dynamics provide information on important biological processes.[1] Several phase imaging methods have been investigated and applied to measure phase changes in various specimens. Such techniques include noninterferometric methods,[2] digital holographic microscopy,[3] full-field phase microscopy based on a programmable spatial light modulator,[4] Fourier fringe analysis,[5] and Hilbert transform.[6] Recent advances in low-coherence interferometry and optical coherence tomography, also enabled several quantitative phase imaging schemes in reflection.[7–9] Spectral-domain optical coherence phase microscopy[10] (SD-OCPM), developed in our laboratory, employs common-path spectral-domain low-coherence interferometry to achieve highly sensitive detection of phase changes. Owing to the improved sensitivity and speed of spectral-domain optical coherence tomography,[11] SD-OCPM demonstrated subnanometer phase sensitivity with a good reflector and produced quantitative phase images on calibrated targets and biological specimens.

While those phase imaging techniques produce high-contrast images of transparent specimens without the need for exogenous contrast agents, the lack of specificity makes it difficult to understand and interpret the images, especially for complex biological specimens. The contrast provided by the phase images arises from the structural variation in size and refractive index inside the sample, not from the signature of particular molecules. On the other hand, the advent of green fluorescent protein (GFP) and its derivatives has significantly reformed fluorescence microscopy and its use in cell biology because of the availability of the intrinsic fluorescent specimens and its much lower phototoxicity.[12] The integration of fluorescence imaging capability with a quantitative phase contrast method therefore not only provides a means to interpret the quantitative phase images but also offers complementary information on the composition and functions of the specimen. Recently, intensity-based optical coherence microscopy was combined with multiphoton microscopy[13,14] (MPM), and diffraction phase and fluorescence microscopy was also demonstrated in transmission.[15]

In this Letter we present simultaneous quantitative phase contrast and multiphoton imaging by use of combined SD-OCPM and MPM (SD-OCP–MPM). For quantitative phase imaging, we demonstrate subnanometer spatial and temporal phase sensitivity of the combined instrument and present MPM and OCPM images simultaneously obtained on stained cells.

The experimental setup of SD-OCP–MPM is depicted in Fig. 1. A broadband 800 nm Kerr-lens mode-locked laser (~130 nm FWHM, FemtoLasers, Austria) is employed for high-resolution OCPM, and a tunable Ti:sapphire pulsed laser with a pulse duration of ~140 fs and a 90 MHz repetition rate (Chame-
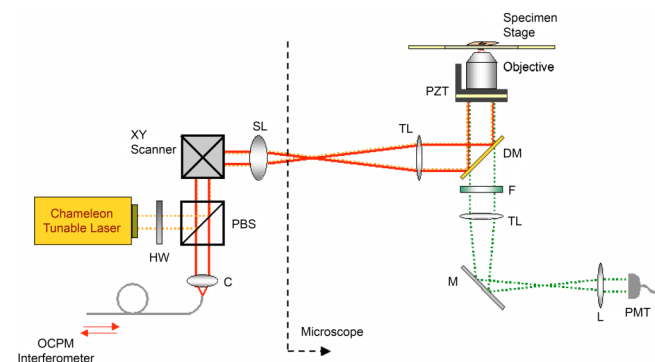

Fig. 1. (Color online) Schematic of SD-OCP/MPM. HW, half-wave plate; C, collimator; SL, scan lens; TL, tube lens; DM, dichroic mirror; F, filter; M, mirror; L, lens.

© 2007 Optical Society of America

leon, Coherent Inc., California) is used for MPM imaging. The solid and dashed lines represent the beam path for OCPM and MPM, respectively. The half-wave plate in front of the Chameleon tunable laser combined with the polarizing beam splitter offers a means to control the beam power at the specimen $(1-10 \text{ mW})$. Combined at the polarizing beam splitter (PBS), both OCPM and MPM beams pass through the XY beam scanners and are introduced to the inverted microscope (Axiovert 200, Carl Zeiss) through its back port. The beams are then magnified by a telescope composed of the scan and tube lenses and are delivered to the specimen through the microscope objective (NeoFluar $20\times$, NA 0.5, Carl Zeiss). For OCPM imaging, the reflection from the bottom surface of a coverslip serves as the reference, whereas the backscattered waves from the focal volume inside the specimen are the measurement fields. The backscattered beams are reflected by the dichroic mirror and coupled back to the fiber for the interference spectrum measurement. The measured spectrum is then Fourier transformed to obtain intensity and quantitative phase information at the focal location, and SD-OCPM generates the structural and phase images of the specimen, as the beam scans the specimen with the galvanometer XY scanners and the piezoelectric transducer (PZT). The lateral resolution of SD-OCPM was measured as 0.75 μm FWHM by imaging a U.S. Air Force resolution target, and the axial resolution, which is the combination of confocal and coherence gatings,[16] was found to be 2.58 μm through the measurement of the intensity at the corresponding depth as a mirror surface moves along the optical axis.

In the case of MPM imaging, the photons emitted in the backward direction are collected by the microscope objective and are transmitted through the dichroic mirror and the filter chosen for a desired emission wavelength. The beam is then guided to the side port of the microscope and detected at the photomultiplier tube (PMT). Our MPM setup operates in photon-counting mode for a high signal-to-noise ratio (SNR), and the dark count rate was measured as 128 Hz. The resolution of MPM was characterized by imaging fluorescent microspheres (0.02 μm in diameter) immobilized in agarose gel and was found to be 0.7 and 4.8 μm in lateral and axial resolution, respectively.

Compared with our previous report,[10] SD-OCP–MPM is built into an inverted microscope and equipped with a 3D scanner for 3D imaging of the biological specimen. The phase stability of SD-OCP–MPM was characterized both spatially and temporally. To examine the spatial phase stability, we obtained two phase images of a coverslip and took the difference between those maps to obtain repeatability of our phase measurement. Figure 2(a) shows the phase repeatability map, of which the field of view is 42 μm × 42 μm with 100×100 pixels. The standard deviation across the field of view was measured as ~0.5 nm in air, which may be in part attributed to the motion jitter of the scanners. For the temporal phase stability, the phase fluctuation was recorded as
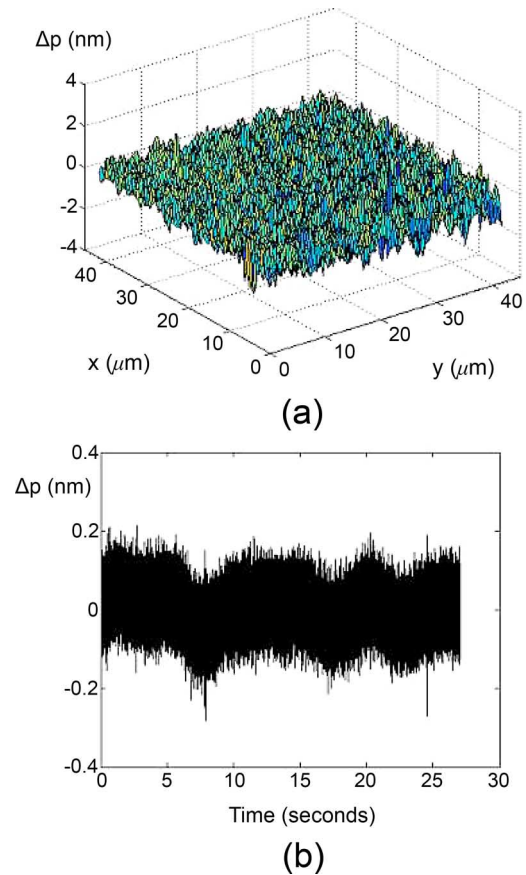

(a)

(b)

Fig. 2. (Color online) Spatial and temporal phase stability of SD-OCP–MPM. (a) The 2D phase repeatability map demonstrates $\sigma \sim 0.5$ nm repeatability in air. (b) Phase fluctuation for a stationary beam; the standard deviation was 53 pm at a SNR of 63.4 dB.

all X, Y, and Z scanners are set to a fixed value (0 V) [Fig. 2(b)]. The measured phase stability was ~53 pm in air at a SNR of 63.4 dB. The theoretical sensitivity is expected to be ~30 pm at the measured SNR, and the difference may be due to external disturbances such as vibration during the measurement.

The simultaneous quantitative phase and multi-photon imaging capability was assessed by imaging prepared muntjac skin fibroblast cells (FluoCells 6, Invitrogen, California). The center wavelength of the MPM tunable source was set to 800 nm. The pixel rate or A-line rate was 10 kHz, and the total acquisition time was ~5 s for an image size of 232 × 232 pixels. Figure 3 shows the images acquired by SD-OCP–MPM at a depth of ~2 μm above the coverslip. The two-photon fluorescence (TPF) image [Fig. 3(a)] clearly shows the distribution of actin filaments inside the cells, labeled with Alexa Fluor 488. The two-photon excitation in nuclei labeled with TO-PRO-3 was not observed because the two-photon absorption cross section of the flurophore is low at the wavelength used for imaging. Figures 3(b)–3(d) represent the intensity, phase, and phase difference images of the same cells, respectively. The phase difference image was obtained by taking the 2D gradient of the phase image and adding the vectors in each pixel, thereby giving a projection view at 45°. Note the ex-
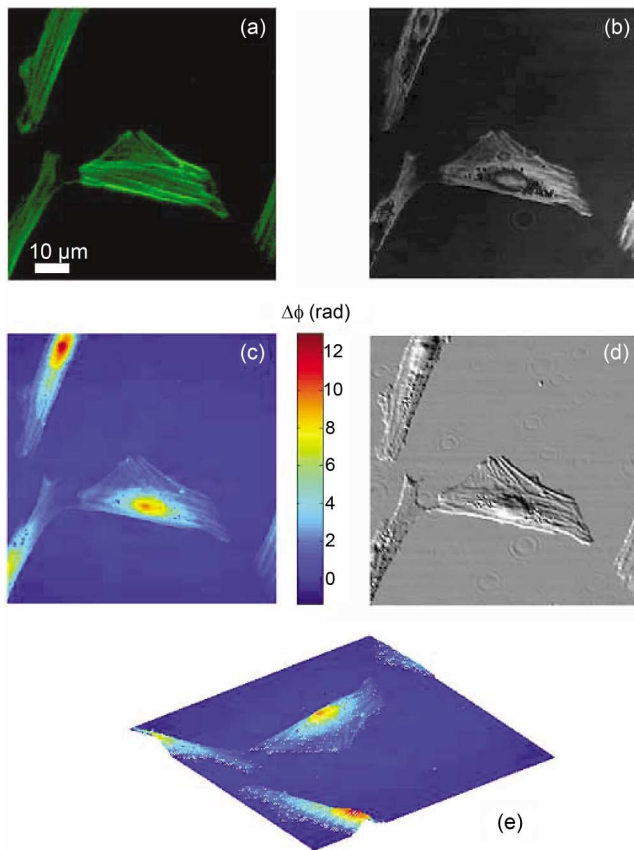
Fig. 3. Images of fixed and stained muntjac skin fibroblast cells. (a) The TPF image shows the distribution of actin filaments labeled with Alexa Fluor 488 phalloidin. (b) Intensity and (c) quantitative phase contrast images obtained in reflection with SD-OCPM. The color bar to the right of the phase contrast image denotes the phase distribution in radians. (d) Computed phase difference and (e) 3D representation of the phase image. The scale bar represents 10 μm.

cellent correlation between TPF and the quantitative phase images in terms of actin filament distribution. This suggests label-free visualization of actin filaments by SD-OCPM and may open up the opportunity for the quantitative studies on actin filament dynamics without fluorescent markers. The nuclei and other subcellular structures were observed in SD-OCPM images, but not in the TPF image. Figure 3(e) shows the 3D representation of the phase image.

Simultaneous SD-OCP–MPM imaging with the broadband OCPM laser source can also be done. However, pulse broadening of the OCPM laser by a long fiber to the microscope and the low power at the specimen did not provide efficient two-photon absorption in our case. The use of the Chameleon source for quantitative phase imaging may not be desirable because its long coherence gating ($\sim$42 μm) does not enable us to resolve and to obtain reliable phase information of the features inside the specimen.

In summary, a multimodal microscope capable of simultaneous quantitative phase contrast and multi-

photon imaging was developed by incorporating MPM capability into the SD-OCPM. Implemented into an inverted microscope, SD-OCP–MPM is characterized by subnanometer phase stability and is applied to image the fixed and stained muntjac skin fibroblast cells. Our results showed that the actin filament distribution in the quantitative phase and the computed phase difference images agreed with that observed in the TPF image. The phase contrast images also revealed the quantitative information of unstained subcellular structures, which can be used as complementary information in biological studies.

References

1. K. Svoboda, C. F. Schmidt, B. J. Schnapp, and S. M. Block, Nature **365**, 721 (1993).
2. A. Barty, K. A. Nugent, D. Paganin, and A. Roberts, Opt. Lett. **23**, 817 (1998).
3. P. Marquet, B. Rappaz, P. J. Magistretti, E. Cuche, Y. Emery, T. Colomb, and C. Depeursinge, Opt. Lett. **30**, 468 (2005).
4. G. Popescu, L. P. Deflores, J. C. Vaughan, K. Badizadegan, H. Iwai, R. R. Dasari, and M. S. Feld, Opt. Lett. **29**, 2503 (2004).
5. S. Kostianovski, S. G. Lipson, and E. N. Ribak, Appl. Opt. **32**, 4744 (1993).
6. T. Ikeda, G. Popescu, R. R. Dasari, and M. S. Feld, Opt. Lett. **30**, 1165 (2005).
7. H. G. Rylander, D. Dave, T. Akkin, and T. E. Milner, Opt. Lett. **29**, 1509 (2004).
8. M. Sticker, M. Pircher, E. Gotzinger, H. Sattmann, A. F. Fercher, and C. K. Hitzenberger, Opt. Lett. **27**, 1126 (2002).
9. M. V. Sarunic, S. Weinberg, and J. A. Izatt, Opt. Lett. **31**, 1462 (2006).
10. C. Joo, T. Akkin, B. Cense, B. H. Park, and J. F. de Boer, Opt. Lett. **30**, 2131 (2005).
11. N. Nassif, B. Cense, B. H. Park, S. H. Yun, T. C. Chen, B. E. Bouma, G. J. Tearney, and J. F. de Boer, Opt. Lett. **29**, 480 (2004).
12. D. W. Pierce, N. Hom-Booher, and R. D. Vale, Nature **388**, 338 (1997).
13. E. Beaurepaire, L. Moreaux, F. Amblard, and J. Mertz, Opt. Lett. **24**, 969 (1999).
14. C. Vinegoni, T. Ralston, W. Tan, W. Luo, D. L. Marks, and S. A. Boppart, Appl. Phys. Lett. **88**, 053901 (2006).
15. Y. Park, G. Popescu, K. Badizadegan, R. R. Dasari, and M. S. Feld, Opt. Express **14**, 8263 (2006).
16. J. A. Izatt, M. R. Hee, G. M. Owen, E. A. Swanson, and J. G. Fujimoto, Opt. Express **19**, 590 (1994).